International Journal of Applied Earth Observations and Geoinformation 117 (2023) 103188

Contents lists available at ScienceDirect

International Journal of Applied Earth Observations and Geoinformation

journal homepage: www.elsevier.com/locate/jag

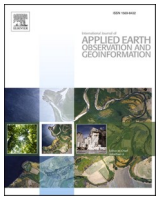

A data-driven approach to flag land-affected signals in satellite derived water quality from small lakes

Dalin Jiang [a,*], Jorrit Scholze [b], Xiaohan Liu [c], Stefan G.H. Simis [c], Kerstin Stelzer [b], Dagmar Müller [b], Peter Hunter [a], Andrew Tyler [a], Evangelos Spyrakos [a]

[a] Earth and Planetary Observation Sciences (EPOS), Biological and Environmental Sciences, Faculty of Natural Sciences, University of Stirling, Stirling, United Kingdom
[b] Brockmann Consult, Hamburg, Germany
[c] Plymouth Marine Laboratory, Plymouth, United Kingdom

ARTICLE INFO

Keywords:
Land-affected signal
Adjacency effects
Optical water type
Inland waters
Water quality

ABSTRACT

The land-affected signal in remotely sensed radiance from nearshore waters is a common problem for remote sensing, introducing uncertainty in atmospheric correction and subsequent water quality constituent concentration estimates. This study proposes a new method for identifying effects of land on satellite remote sensing of water quality. The new optical water types (OWT) containing the land-affected signal were derived from POLYMER-corrected imagery of the Medium Resolution Imaging Spectrometer in reduced resolution (MERIS RR) and Sentinel-3 Ocean and Land Colour Instrument (OLCI). These were then applied, as part of a larger set of existing OWTs corresponding to the variability observed in natural waters, to satellite images. The ability to identify pixels containing both water and land, and those contaminated with radiance from adjacent land, was evaluated. Our test sites include dark lakes of varying size in Sweden (Lakes Rusken, Bolmen, Ringsjön, and Ivösjön) where the classification showed high sensitivity to land near the lake shore. The land-affected signal is shown to lead to underestimations of chlorophyll-a concentration and Forel-Ule colour indices, and overestimations of turbidity in these lakes, which can be corrected after masking out the land-affected pixels. The land-affected signal is strongest in summer, both NDVI and sun zenith angle covaried with the seasonal variation of land-affected signal. Further, the results confirmed that satellite images with coarser spatial resolution are more prone to land-affected signal compared to images with finer spatial resolution, for small inland water bodies. We propose a data-driven approach for water quality processing with 'land-affected water types' as an effective way to improve the lake optical water quality monitoring from water colour sensors.

1. Introduction

Nearshore waters are important habitat for fish, fowl, and other wildlife, and provide ecosystem services that are fundamental to societal wellbeing (Edsall & Charlton, 1997; Vadeboncoeur et al., 2011). Nearshore waters are subject to multiple conflicting societal and economic demands. They are often under pressure from multiple anthropogenic activities, such as fishing, transportation, construction of power plants, dredging, and discharge of pollutants (Edsall & Charlton, 1997; Blaber et al., 2000; Jägerbrand et al., 2019). Satellite-based Earth observation (EO) methods can improve our understanding of these systems and provide actionable information to support conservation and management solutions. However, monitoring of nearshore waters from optical remote sensors is challenging due to a variety of reasons including complex shoreline morphologies, optically shallow water, and vegetation. Mixing of light reflected from the water column with light reflected from adjacent land, sensitivity to the composition of the atmosphere above water bodies, and the geometry of incident light and sensor field-of-view can also challenge remote sensing applications in nearshore waters.

These challenges are often linked with contamination of the remotely sensed signal by land surfaces nearby. We can distinguish two ways in which the land signal might interface with remote sensing of water surfaces. The first is where land presents at a subpixel scale within a pixel associated with water (Yamazaki et al., 2015; Klein et al., 2017). This is challenging to determine due to the dynamic nature of water extend and the spatial resolution (typically 300 m) of water colour sensors. We refer to this as the "land–water mixed pixel" problem. The

* Corresponding author.
E-mail address: dalin.jiang@stir.ac.uk (D. Jiang).

https://doi.org/10.1016/j.jag.2023.103188
Received 12 September 2022; Received in revised form 3 December 2022; Accepted 11 January 2023
Available online 17 January 2023

second is mixing of sunlight reflected by land and in water column, which occurs in the atmosphere. The degree of mixing contaminates with the signal from water depends on many factors such as the contrast between land and water albedo (wavelength dependent), distance to land, aerosol abundance and types, land cover type, view and sun geometries (Santer & Schmechtig, 2000; Bulgarelli & Zibordi, 2018; Bulgarelli et al., 2018). We call this "land-adjacency effect". We refer to the land–water mixed pixel problem and land-adjacency effect collectively as "land-affected signal" problem in this study, and those pixels suffering from the land-affected signal are referred to as "land-affected pixels". Inland waters, especially small aquatic systems, are susceptible to land-affected signals, which can lead to errors in atmospheric correction, and consequently in the derived remote sensing products (Santer & Schmechtig, 2000; Giardino et al., 2007; Bulgarelli et al., 2018).

Various studies have proposed procedures to minimize or remove the land-affected signal over inland and coastal waters. Some studies suggest to exclude pixels within a fixed distance from the shoreline, to reduce the influence from land-water mixed pixels and, to some extent, adjacency effects (Wang et al., 2018; Jiang et al., 2019). However, these approaches are not selective and can also remove water pixels which are not affected by land. Moreover, adjacency effects are not only limited to a few pixels from the shore but can be detected several kilometres offshore in inland and coastal waters. Other methods attempt to identify and flag the pixels influenced by adjacency effects. For example, Matthews and Odermatt (2015) proposed to flag pixels affected heavily by adjacent land using empirically determined thresholds of maximum peak height (MPH) and normalized difference vegetation index (NDVI), and the position of the reflectance peak in the near-infrared (NIR) wavelengths. Some approaches attempt to remove the adjacency effects from satellite images. Sterckx et al. (2015) proposed the SIMilarity Environment Correction (SIMEC) for adjacency effects correction for Medium Resolution Imaging Spectrometer (MERIS) data. SIMEC is based on the NIR similarity spectrum and corrects the adjacency effects before implementing an atmospheric correction algorithm. Kiselev et al. (2015) suggested an algorithm for correcting adjacency effects, which is based on the point spread function (PSF) and can be applied to any satellite or airborne sensors' data. Despite these efforts, lack of predictability and independent observations to bound the problem still hinders the application of remote sensing for monitoring nearshore waters.

The magnitude and shape of the water reflectance spectrum in the visible and infrared contain information on key-coloured substances such as phytoplankton pigments, organic and inorganic suspended particulates, and dissolved compounds (Kirk, 1984). Optical water type (OWT) classification has been suggested over the last forty years (Jerlov, 1977; Morel & Prieur, 1977) as a mechanism to delineate water masses in oceanic, coastal and inland systems based on their optical properties. For example, Moore et al. (2014) classified seven OWTs to show that blending OC4 and 3-band MERIS algorithms assigned as a function of OWT membership can improve chlorophyll-*a* (Chl-a) retrieval accuracy. Wei et al. (2016) identified 23 OWTs based on in situ water reflectance spectra, which was applied to assess the quality of in situ reflectance spectra. Spyrakos et al. (2018) identified 13 OWTs for inland waters and 9 OWTs for coastal waters based on in situ measured reflectance spectra. OWT classification can act as a guide to select the most suitable water quality retrieval algorithm for a specific water type in EO applications. It has been shown that blended algorithms based on OWT classification can improve the retrieval accuracy of water quality indicators, like Chl-a concentration (Matsushita et al., 2015; Neil et al., 2019; Cui et al., 2020; Liu et al. 2021), water transparency (Jiang et al., 2019; Qing et al., 2021), and total suspended solids concentration (Balasubramanian et al., 2020; Jiang et al., 2021).

In the same way that OWTs describe how biogeochemically relevant substance concentrations form naturally occurring clusters of water colour, it may be assumed that the land-affected signal introduces variations in the perceived water colour. Whilst the mixing of these signals in the atmosphere can be physically formulated, it is not known how the contaminated water-leaving radiance appears following atmospheric correction of optical imagery, which is a common step in the interpretation of satellite imagery of water quality. This study aims to characterise the propagation of the land-affected signal throughout the water quality processing chain in order to exploit potential systematic behaviours. Specifically, land-affected signals could be flagged by extending the existing OWT classification to include major or subtle OWT variations introduced by land. Here, we use water-leaving reflectance (R_w) from the European Space Agency (ESA) Climate Change Initiative Lake (Lakes_cci) product, which were derived with POLYMER atmospheric correction (Steinmetz et al., 2011; Simis et al., 2020). The analysis is performed over a series of low reflectance boreal lakes, where brownification has been reported (Klante et al., 2021; Arzel et al., 2020; Taipale et al., 2016). Contamination of water colour observations by land is particularly relevant in dark lakes (high land/water contrast) and requires adequate data masking in order to monitor brownification over long periods using multiple satellite sensors.

The specific objectives of this study are to: (1) analyse R_w over a gradient of high to low influence of land-affected signals in inland water remote sensing images, and identify typical spectral signature which can be adopted as new OWTs for the land-affected signal; (2) use the newly identified OWTs for the land-affected signal to flag and mask land-affected observations; (3) explore the influence of the land-affected signal on water colour and subsequent water quality variable retrievals.

2. Data and methodology

2.1. Study area

This study mainly focused on four lake areas in southern Sweden: lakes Rusken, Bolmen, Ringsjön and Ivösjön (Fig. 1). These lakes have a minimum water surface area of 34 km^2 (Lake Rusken), and a maximum area of 171 km^2 (Lake Bolmen). Islands are present in Lake Rusken, mainly in the southern part (Fig. 1a). Lake Bolmen surrounds the large Bolmsö island and has additional smaller islands in the central and northern parts of the lake (Fig. 1b). Lake Ringsjön consists of a western part and an eastern part connected by a narrow waterway, and in contrast to other lakes in this study, there is only one small island in the western part of this lake (Fig. 1c). Lake Ivösjön is divided into two basins with a large island in the centre of the eastern part of the lake (Fig. 1d). Among the studied lakes, shorelines of Lake Ringsjön are relatively less complex than other lakes. The main land cover types around the studied lakes are forest and arable land (O'Dwyer, 2019; Klante et al., 2021).

2.2. In situ data

We used in situ Chl-a data to assess the impact of the land-affected signal on Chl-a concentration estimates. Chl-a concentration records for water samples from lakes Bolmen and Ringsjön during 2002 and 2019 were retrieved from the Miljödata MVM database (https://miljodata.slu.se/MVM/). Satellite matchups were defined as measurements of in situ data on the same day of the satellite overpass. This resulted in 76 Chl-a matchups, of which 68 matchups were from three stations in Lake Ringsjön (Fig. 1c) and 8 matchups measured at two stations in Lake Bolmen (Fig. 1b).

2.3. Satellite data

We used the R_w, Chl-a concentration, turbidity, and land–water fraction (LWF) data from an intermediate product of Level-2 ESA Lakes_cci version 1.0 product for lakes Rusken, Bolmen, Ringsjön and Ivösjön. L3S daily aggregated 1-km reprojection of this dataset is available through the Lakes_cci (https://climate.esa.int/en/projects/lakes/data/). The Calimnos processing chain was employed for the processing of the Medium Resolution Imaging Spectrometer reduced

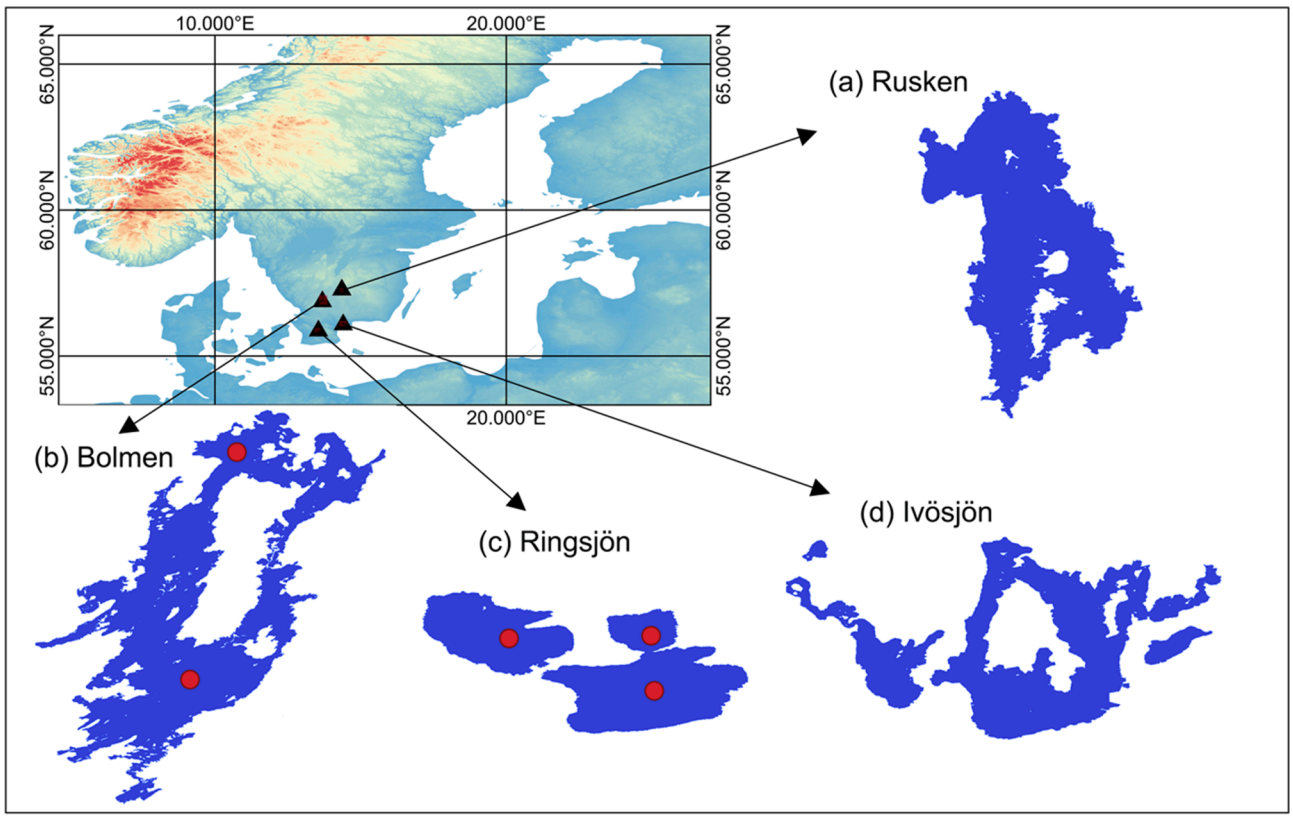

Fig. 1. The studied lakes in Sweden: (a) Lake Rusken, (b) Lake Bolmen, (c) Lake Ringsjön, (d) Lake Ivösjön. Red points in lake Bolmen and Ringsjön represent the monitoring site of in situ data. (For interpretation of the references to colour in this figure legend, the reader is referred to the web version of this article.)

resolution (MERIS RR) with a ~ 1.2 km and Sentinel-3 Ocean and Land Colour Instrument (OLCI) with a ~ 300 m on-ground resolution at sub-satellite point. The MERIS RR was used rather than MERIS full resolution (MERIS FR), because MERIS RR has better global coverage particularly during the first years of the mission (Odermatt et al., 2018). The specific algorithms for R_w and the derived water quality products are described in Simis et al. (2020) and Liu et al. (2021). Briefly, POLYMER v4.12 atmospheric correction (Steinmetz et al., 2011) was applied to MERIS RR (2002–2012) and OLCI (2016–2019) images to yield R_w values. Chl-a and turbidity products were derived based on weighted blending of water constituent algorithms tuned to each OWT (Spyrakos et al., 2018; Neil et al., 2019). R_w from lakes Rusken and Bolmen were used to develop the OWT-based land-affected signal flagging framework, while its applicability was tested in an independent R_w dataset from lakes Ringsjön and Ivösjön. Chl-a concentration and turbidity data were used to assess how these are affected by the land-affected signal.

LWF data describes the fraction of water coverage (with 0 for land, 100 for water, and value in between for land–water mixed pixels), which was determined from the Shuttle Radar Topography Mission (SRTM, Farr et al., 2007) and derived using the Land/Water Mask Algorithm from the Sentinel Application Platform (SNAP). This static map was used to assess proximity to land. The Forel-Ule (FU) colour index, with scales from 1 (deep blue) to 21 (yellowish-brown), was calculated for the studied lakes using the method from Woerd et al. (2015) based on R_w, it was used to analyse the influence of the land-affected signal on water colour retrievals.

2.4. Development of flagging method

2.4.1. Selection of data points for spectral analysis

We statistically analysed how the spectral shape and magnitude changed when transitioning from lake centre towards the shore. Based on the size of the lake, and the spatial resolution of MERIS RR and OLCI, we selected either three or four points from lake centre to the shore (P0, *P*1, *P*2, *P*3 in Figs. 2–3), and extracted the R_w of these three (or four) points from all available images between 2002 and 2019.

The colour scale in Figs. 2–3 indicates the LWF (%), a pixel with LWF < 100 % indicates a risk or likelihood of land presence, while a pixel with LWF $= 100$ % means the pixel only includes water. The selected points in both lakes represent water pixels with high LWF at lake centre and land–water mixed pixels with low LWF near the lake shore, thus to cover a gradient of low to high influence from the land-affected signal.

2.4.2. Development of new OWTs for the land-affected signal

The 13 OWTs developed for inland waters by Spyrakos et al. (2018) were included in the Lakes_cci product, and used in Chl-a concentration and turbidity retrievals (Simis et al., 2020; Liu et al., 2021). In this study, we identified two new OWTs for the land-affected signal and extended the existing 13 OWTs to 15 OWTs. We named these two OWTs OWT-14 and OWT-15 for collective application purpose with the existing OWTs. To explore the spectral signature variations from lake centre to lake shore, we analysed the MERIS RR and OLCI R_w extracted from lakes Rusken and Bolmen described in section 2.4.1, and their covariation with LWF. Based on the above analysis, it was assumed that pixels with 0 %<LWF < 100 % are more likely subject to the land-affected signal. To determine the typical spectral shape of new OWTs for the land-affected signal, we firstly extracted the spectra of all pixels with 0 %<LWF < 100 % from all MERIS RR and OLCI images for Lakes Rusken and Bolmen. We then standardized these extracted spectra with a division by the area between the spectrum and a zero baseline (Spyrakos et al., 2018). The new OWTs were determined as the median value of the standardized spectra from MERIS RR (OWT-14) and OLCI (OWT-15), respectively.

2.4.3. Framework of flagging the land-affected signal

For a given atmospherically corrected satellite image pixel, the OWT-based land-affected signal flagging method proposed in this study in-

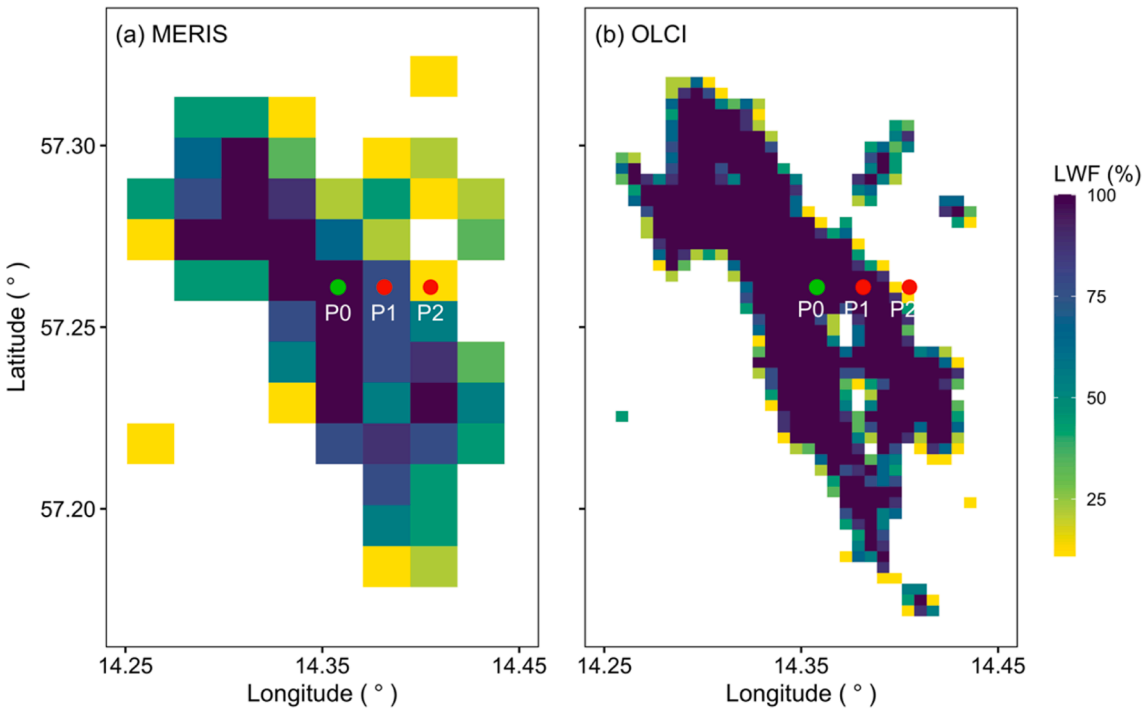

Fig. 2. Locations for spectral analysis in Lake Rusken, P0–*P*2 represent the selected points from lake centre to lake shore. (a) Locations shown on MERIS RR image. (b) Locations shown on OLCI image. Colour indicates the land–water fraction.

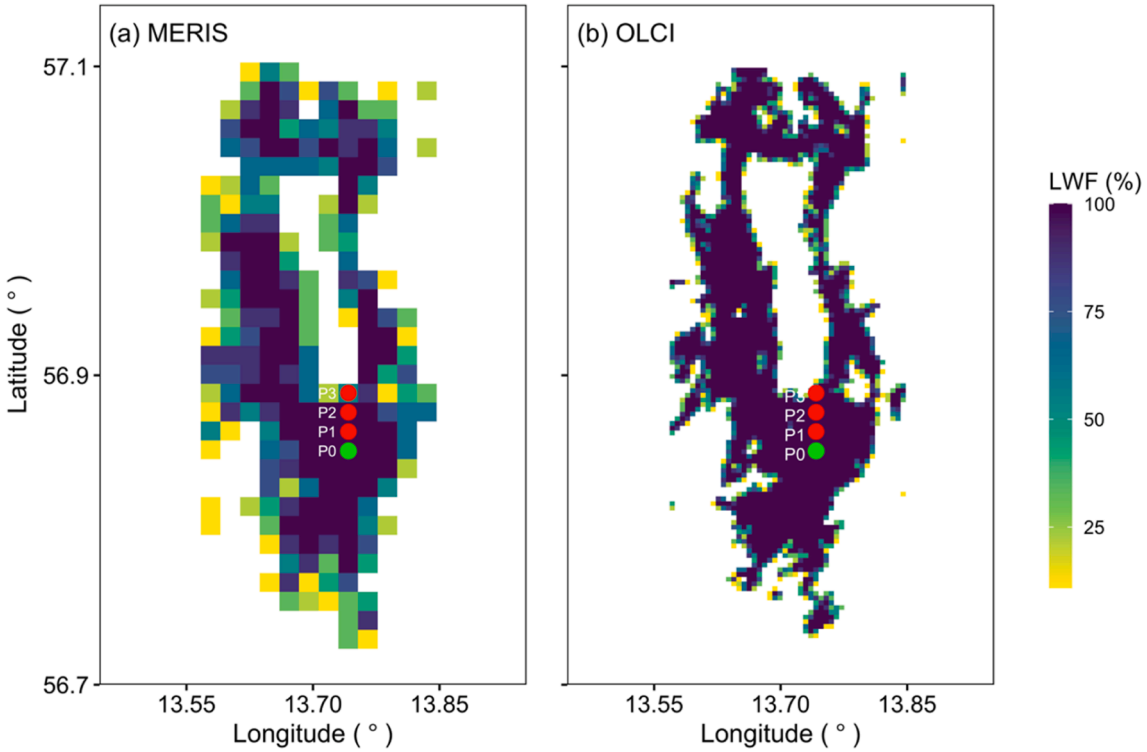

Fig. 3. Locations for spectral analysis in Lake Bolmen, P0–*P*3 represent the selected points from lake centre to lake shore. (a) Locations shown on MERIS RR image. (b) Locations shown on OLCI imagery. Colour indicates the land–water fraction.

cludes three main steps:

(1) Standardize the R_w spectrum with a division by the area between the spectrum and a zero baseline.

(2) Calculate OWT membership score based on spectral angle between the standardized R_w spectrum and each of the 15 OWTs using the following equations:

$$\alpha = cos^{-1}\frac{\sum_{i=1}^{n} p_i r_i}{\sqrt{\sum_{i=1}^{n} p_i^2}\sqrt{\sum_{i=1}^{n} r_i^2}} \quad (1)$$

$$S_{OWT} = 1 - \alpha/\pi \quad (2)$$

where p_i is the reflectance in band i for the satellite image pixel, and r_i is the reflectance in band i for the reference OWT spectrum, α is the spectral angle between a satellite image spectrum and a reference OWT spectrum in radians. S_{OWT} is OWT membership score in a range of zero to one, where one implies an identical spectral shape.

(3) The OWT corresponding to the maximum S_{OWT} is identified as the optical water type for this pixel.

Repeating the above steps for all pixels, will create a new image layer with OWTs from 1 to 15, where pixels without the land-affected signal will be in between OWT-1 and OWT-13, and pixels with the land-affected signal will be identified as OWT-14 or OWT-15. A new mask layer with binary value can also be created based on the OWT layer. For example, users can assign the value of pixels which show OWT-1 to OWT-13 to 1, and assign the value of pixels which show OWT-14 or OWT-15 to 0. This mask layer could be used to exclude observations with potential influence from the land-affected signal.

2.4.4. Analysis of the land-affected signal and its impact on water quality retrievals

To study the spatial distribution of land-affected signals, we calculated the land-affected signal frequency index (LSI) for each pixel in each lake based on the results of applying the flagging framework in section 2.4.3 to all MERIS RR and OLCI images. For each pixel in a lake, the LSI is calculated as:

$$LSI = \frac{N_L}{N_T} \times 100 \quad (3)$$

where N_L is the number of images influenced by the land-affected signal (OWT-14 or OWT-15) and N_T is the number of total valid images for this pixel. LSI reflects the frequency of one pixel being flagged as land-affected in a lake, its value ranges from 0 % to 100 %, with a higher value implying more often affected by the land-affected signal. To explore the seasonal variability of land-affected signal, we calculated the mean LSI values for four seasons (Spring: March–May, Summer: June–August, Autumn: September–November, and Winter: December–February) in all studied lakes.

Impacts of the land-affected signal on the retrieval of water colour and water quality variables were firstly assessed by validating Chl-a retrievals with in situ data, and then assessed by comparing the statistics of lake average Chl-a concentration, turbidity and FU value before and after masking out land-affected pixels.

3. Results

3.1. R_w spectra from lake centre to shore

Distinct changes in spectral magnitude and shape can be observed when transitioning from lake centre to the shore in Lake Rusken (Fig. 4) and Lake Bolmen (Fig. 5). The spectral magnitude at lake centre is generally low in the two lakes for both MERIS RR (Fig. 4a, 5a) and OLCI (Fig. 4d, 5e) images, and the magnitude of spectra increases gradually from lake centre to lake shore in the two lakes for both MERIS RR (Fig. 4a–4c, Fig. 5a–5d) and OLCI (Fig. 4d–4f, Fig. 5e–5 h). The spectral shape also changes from lake centre to the shore for both sensors. This change is most prominent in the NIR wavelengths (700–800 nm, e.g., Fig. 4c, 4f, 5d, 5 h) where reflectance values increase towards the shore.

In addition, differences in spectral shape of the pixel selected at lake shore can be observed between MERIS RR and OLCI. R_w in the short wavelengths (400–500 nm) from MERIS RR images is higher than those observed from OLCI images (e.g., Fig. 4c vs 4f). R_w in NIR wavelengths (700–800 nm) from MERIS RR imagery is lower than observed from OLCI imagery (Fig. 5d vs 5 h). Despite these differences at the lake shore, the MERIS RR (Fig. 4c, 5d) and OLCI (Fig. 4f, 5 h) spectral shape at lakes Rusken and Bolmen are highly similar between these lakes. The above

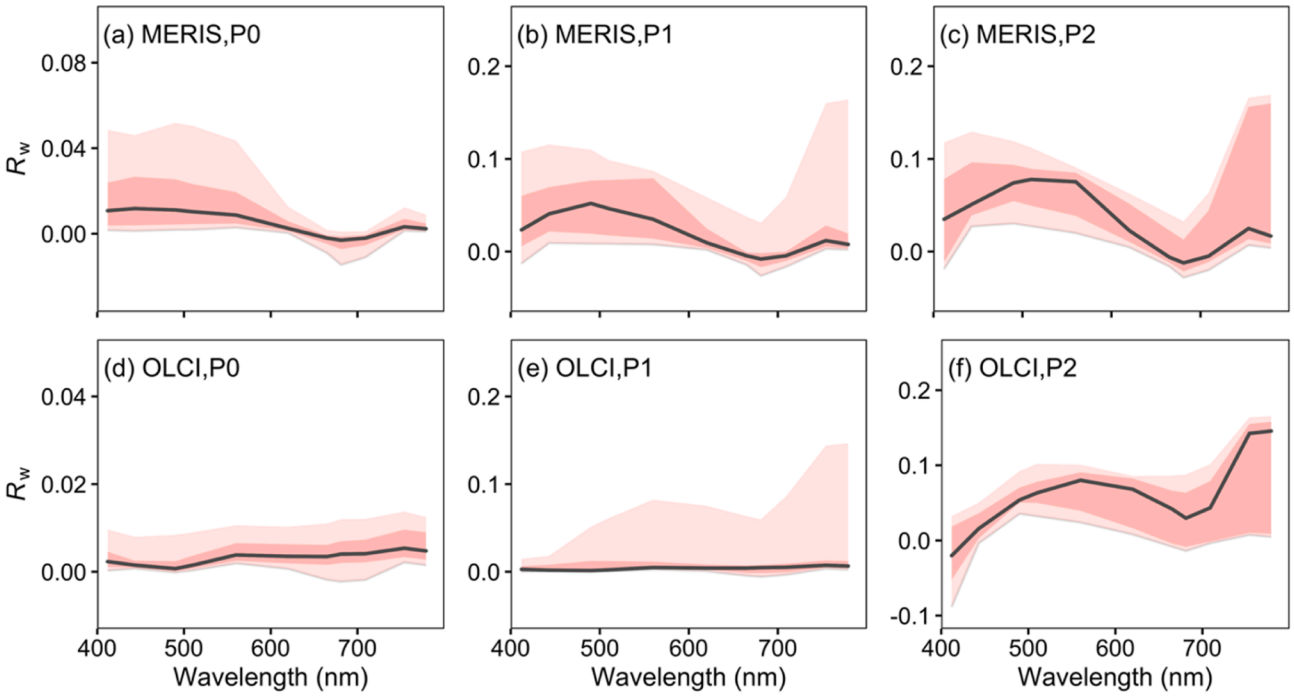

Fig. 4. Spectra at the selected points in Lake Rusken. (a)–(c): Spectra at P0–*P*2 from MERIS RR. (d)–(f): Spectra at P0–*P*2 from OLCI. Black solid line represents median value, red area represents 25%–75% quantiles, and light red area represents 10%–90% quantiles. (For interpretation of the references to colour in this figure legend, the reader is referred to the web version of this article.)

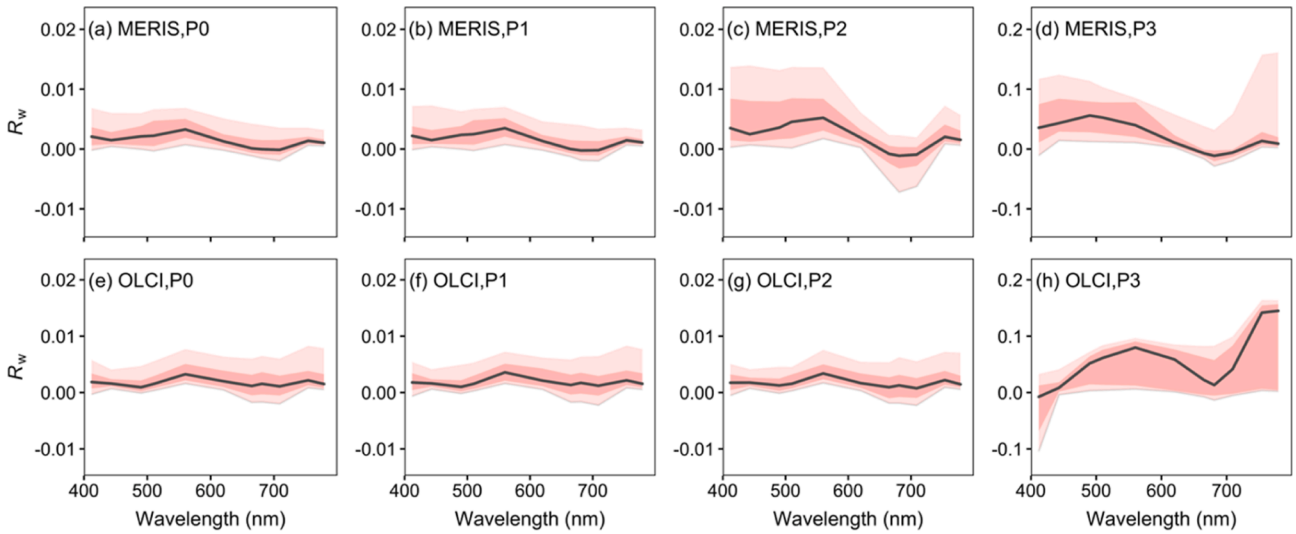

Fig. 5. Spectra at the selected points in Lake Bolmen. (a)–(d): Spectra at P0–*P*3 from MERIS RR. (e)–(h): Spectra at P0–*P*3 from OLCI. Black solid line represents median value, red area represents 25%–75% quantiles, and light red area represents 10%–90% quantiles. (For interpretation of the references to colour in this figure legend, the reader is referred to the web version of this article.)

characteristics show the consistency of spectral shapes at lake shore in the two lakes, and also indicate that the spectra of the land-affected signal should be identified for MERIS RR and OLCI separately.

The LWF value is found to be highly related with the spectral characteristics when moving from lake centre to the shore (Figs. 2–3, and Figs. 4–5). When pixels are located at lake centre with very high LWF values (e.g., P0 in Fig. 2b), R_w is low (Fig. 4d). When pixels are located between lake centre and land with medium LWF values, the magnitude and shape of the spectra change compared to those pixels at lake centre (e.g., *P*1 in Fig. 2b and 4e). In cases of those pixels nearby land with very low LWF values (e.g., *P*2 in Fig. 2b), the spectral magnitude increases significantly and the spectral shape in the NIR changes clearly (Fig. 4f). This suggests that variability in the LWF is reflected in the pixels' spectral shape and magnitude.

3.2. Spectral signature for the land-affected signal

Fig. 6a shows the two new OWTs identified from MERIS RR and OLCI for the land-affected signal. They are the median value of the standardized spectra extracted from pixels with LWF between 0 and 100 % as detailed in section 2.4.2. Fig. 6b shows the top two dominated existing OWTs (47 % of all MERIS RR and OLCI images) from Spyrakos et al. (2018) for the centre of Lakes Rusken and Bolmen. We can see that the shape of the two new OWTs for the land-affected signal are different with the top two existing OWTs in these two lakes in all wavelengths, especially in the NIR. Also, the spectral shape between the two new OWTs for the land-affected signal are different throughout the spectrum, where the standardized R_w of MERIS RR is higher at blue–green bands and lower at red–NIR bands than OLCI, but both spectra showed high reflectance in the NIR wavelengths. We named the new OWT from MERIS RR as OWT-14, and the new OWT from OLCI as OWT-15 as an extension of the 13 existing OWTs from Spyrakos et al., (2018). In applications, when the spectrum of a pixel shows maximum membership with OWT-14 or OWT-15, it will be flagged as a land-affected pixel (section 2.4.3).

3.3. Spatial effects

Land-water mixed pixels close to the lake shore (yellow pixels in Figs. 7 and 8) have, as expected, the highest LSI values. The LSI is also relatively high in pixels located from lake shore to lake centre, but lower than those directly located at the lake shore. The lowest LSI is in the centres of both Lake Rusken and Bolmen. For example, the LSI at P0, *P*1 and *P*2 (same locations as in Fig. 2) in Lake Rusken are 19 %, 32 % and

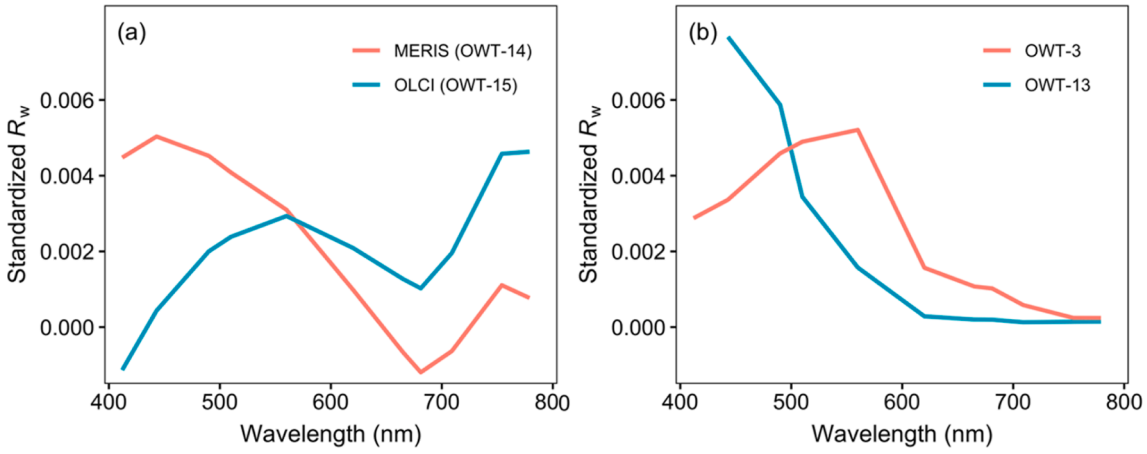

Fig. 6. (a) Typical standardized R_w spectra indicating the presence of the land-affected signal. (b) The spectral shapes of the top two dominating OWTs from Spyrakos et al. (2018) for the centres of Lakes Rusken and Bolmen.

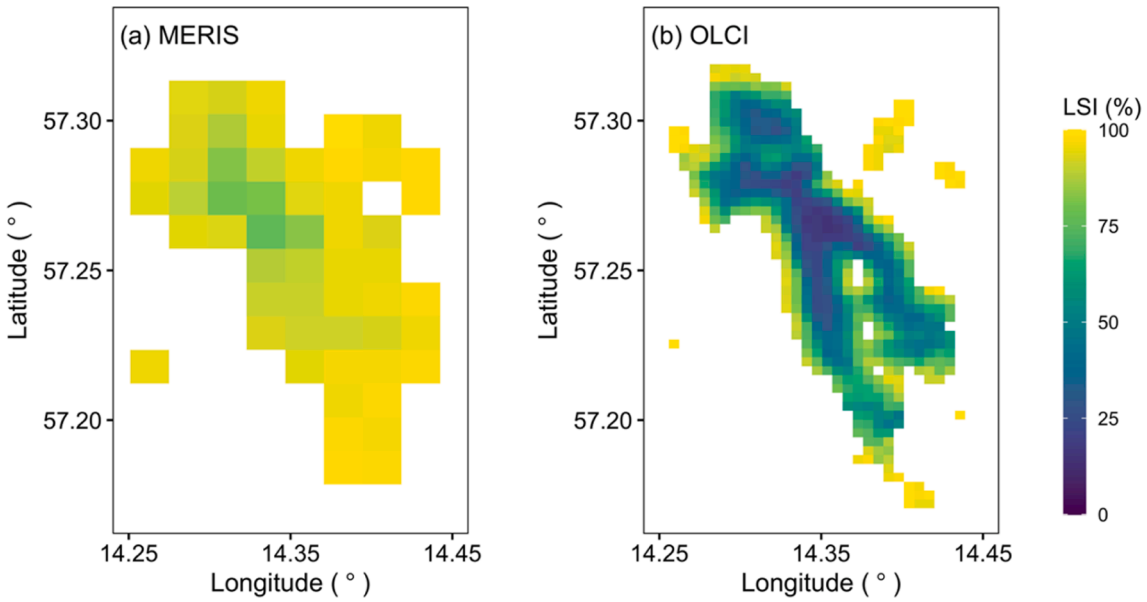

Fig. 7. Land-affected signal frequency maps for Lake Rusken from (a) MERIS RR, (b) OLCI.

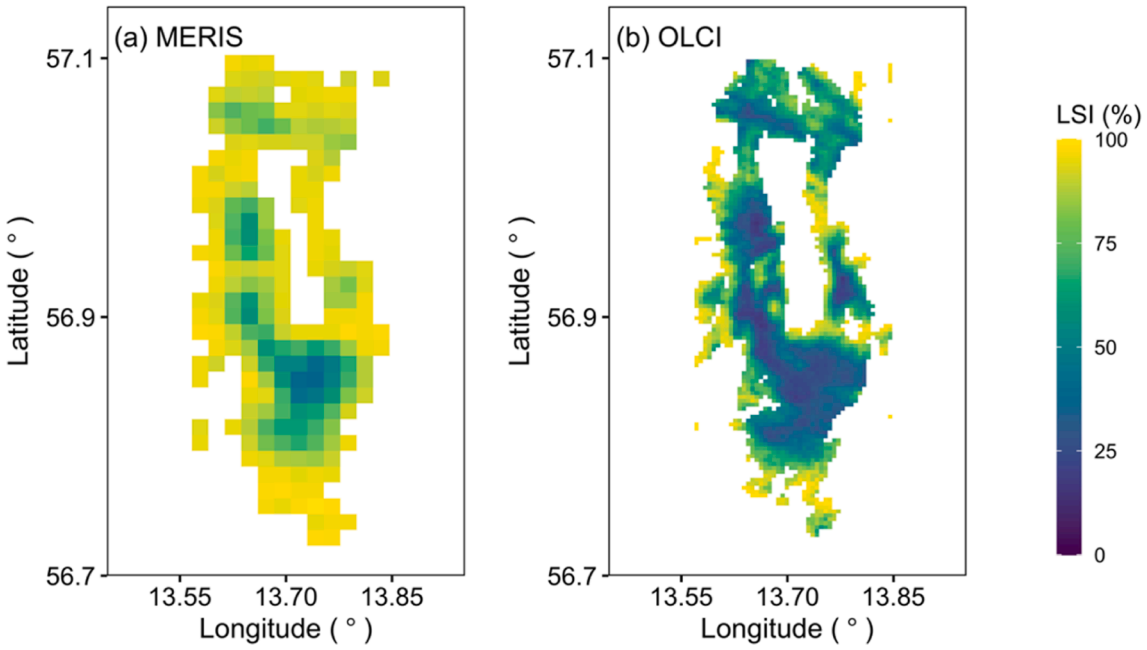

Fig. 8. Land-affected signal frequency maps for Lake Bolmen from (a) MERIS RR, (b) OLCI.

93 % respectively for OLCI. Pixels close to large islands also show high LSI values, such as the pixels close to the two islands in the southern part of Lake Rusken (Fig. 7b). These results indicate that not only land–water mixed pixels, but also pixels with some distance to lake shore are influenced by the adjacent land.

It can be also seen that the LSI maps between MERIS RR and OLCI are different. Overall, the LSI values for MERIS RR are higher than those for OLCI, especially in lake centre. For example, in the centre of Lake Rusken (P0), the LSI values from MERIS RR and OLCI are 83 % and 19 %, respectively. For the centre of Lake Bolmen (P0), the LSI values from MERIS RR and OLCI are 37 % and 27 %, respectively.

Our OWT-based framework is able to capture the land-affected signal in both MERIS RR and OLCI datasets from lakes Ringsjön and Ivösjön. LSI values decrease from the shore to centre gradually for both lakes Ringsjön (Fig. 9) and Ivösjön (Fig. 10). In Lake Ringsjön, the minimum LSI values are 14 % and 3 % for MERIS RR and OLCI, respectively. In Lake Ivösjön, the minimum LSI values are 38 % and 6 % for MERIS RR and OLCI, respectively. It should be noted that the LSI values at the central part of Lake Ringsjön (Fig. 9) are clearly lower than the LSI values at central areas of Lake Ivösjön (Fig. 10), Lake Rusken (Fig. 7) and Lake Bolmen (Fig. 8). Furthermore, LSI spatial patterns are the same between MERIS RR and OLCI with higher LSI at lake shore and lower LSI at lake centre. The overall LSI values are higher for MERIS RR than for OLCI.

3.4. Impact of the land-affected signal on the remote sensing retrieval of water quality variables

We compared the validation results of Chl-a concentration before and after masking out land-affected pixels (i.e., pixels identified as OWT-

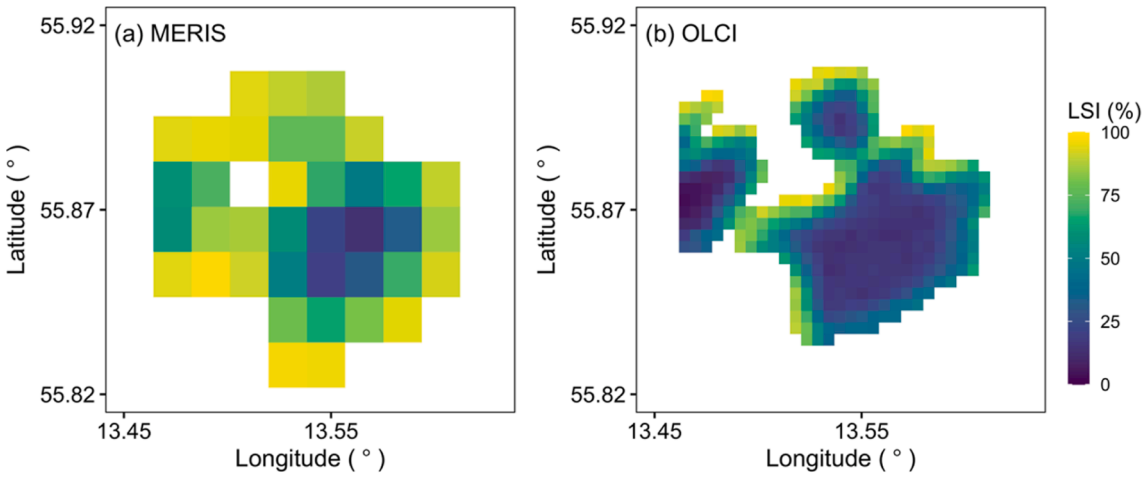

Fig. 9. Land-affected signal frequency maps for Lake Ringsjön from (a) MERIS RR, (b) OLCI.

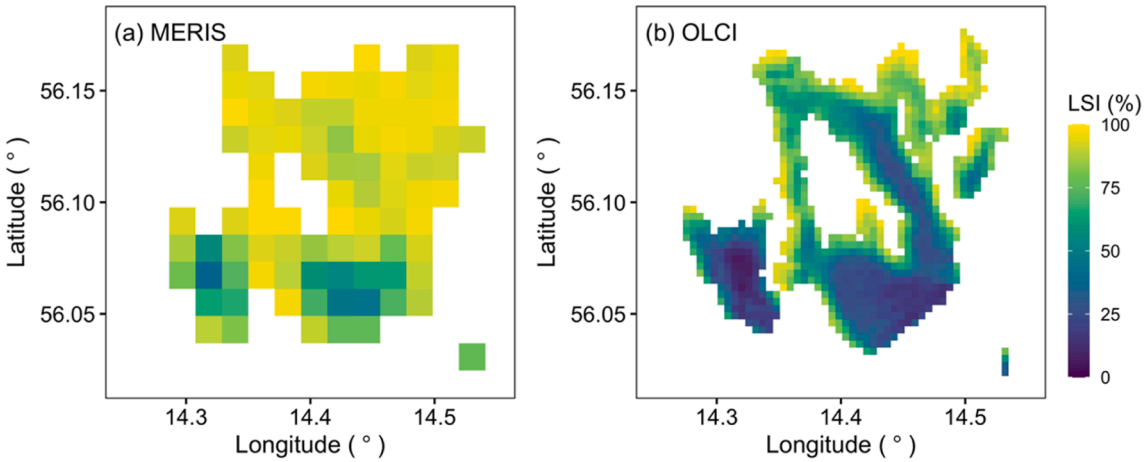

Fig. 10. Land-affected signal frequency maps for Lake Ivösjön from (a) MERIS RR, (b) OLCI.

14 or OWT-15). There are 29 data points identified as OWT-14 or OWT-15 in the matchups. There are many underestimated Chl-a concentrations with a bias of −0.5, which are caused by the influence of adjacent land (red points in Fig. 11a). After masking out land-affected data points, satellite derived Chl-a concentrations are more consistent with in situ measured data (Fig. 11b), with the root mean squared error (RMSE)

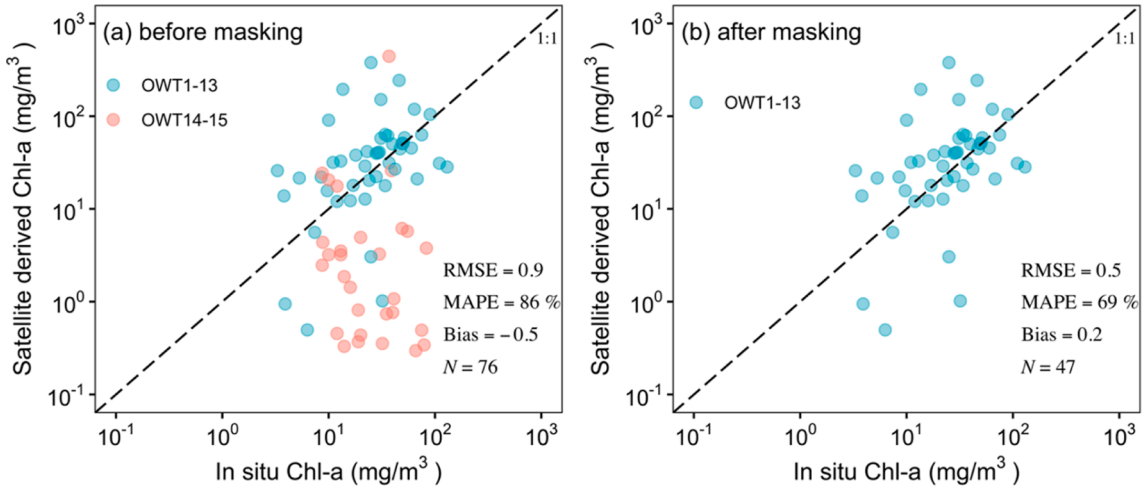

Fig. 11. Comparison and validation of Chl-a concentration derived from satellite images. (a) Validation before masking land-affected pixels, (b) validation after masking land-affected pixels. The original results of 15 OWTs are re-grouped into two groups for better comparison, blue points indicate pixels which are identified as OWT 1–13 without land-affected signals, red points indicate pixels identified as OWT 14 or 15 with land-affected signals. (For interpretation of the references to colour in this figure legend, the reader is referred to the web version of this article.)

decreasing from 0.9 to 0.5 (in log scale), median absolute percentage error (MAPE) from 86 % to 69 %, and an improved bias from −0.5 to 0.2.

Fig. 12 shows the density plots of lake average Chl-a concentration in the studied lakes. There are evident differences in Chl-a concentration before and after masking out land-affected pixels in all lakes. Generally, the lake average Chl-a concentration increases after masking out land-affected pixels. For example, in Lake Rusken, the median Chl-a concentration is 8.6 mg/m^3 before masking, and this value increases to 21.5 mg/m^3 after masking (Fig. 12a). Similarly, the median value of lake average Chl-a concentration increases from 9.0 mg/m^3 to 17.1 mg/m^3 for Lake Bolmen (Fig. 12b), from 17.9 mg/m^3 to 36.3 mg/m^3 for Lake Ringsjön (Fig. 12c), and from 10.5 mg/m^3 to 15.9 mg/m^3 for Lake Ivösjön (Fig. 12d).

Contrasting results are found for lake average turbidity before and after masking of land-affected pixels (Fig. 13). A decrease from 21.0 NTU to 5.2 NTU is observed in Lake Rusken after masking out land-affected pixels (Fig. 13a). Similarly, the median turbidity decreases from 18.6 NTU to 4.8 NTU for Lake Bolmen, and from 16.2 NTU to 2.1 NTU for Lake Ringsjön, and from 17.8 NTU to 2.9 NTU for Lake Ivösjön as shown in Fig. 13.

Comparing the lake average FU value after masking out land-affected pixels with the value before masking, it can be found that the FU value increases in all studied lakes (Fig. 14). The increase of FU value is more clear for lakes Rusken and Bolmen than lakes Ringsjön and Ivösjön, with the median value increasing from 6.4 to 13.4 for Lake Rusken (Fig. 14a), and from 6.0 to 11.6 for Lake Bolmen (Fig. 14b). The peaks of FU value change from ~ 4 to ~ 17 for Lake Rusken, and from ~ 4 to ~ 16 for Lake Bolmen, both indicating that the water colour changes from indigo-blue to greenish brown after masking out land-affected pixels. Changes of FU value are relatively small after masking out land-affected pixels for lakes Ringsjön and Ivösjön compared to the other two lakes, but they still increase from 6.8 to 9.9 (Fig. 14c), and from 5.3 to 9.0 (Fig. 14d), respectively. FU peaks also move to higher range but not as high as results for lakes Rusken and Bolmen.

3.5. Seasonal variability of the land-affected signal

LSI reveals a clear seasonal variation for both MERIS RR and OLCI images (Fig. 15), because the LSI values of land–water mixed pixels are always high (Figs. 7–10), the seasonal variation of LSI mainly depends on the change of adjacency effects on the pixels between lake centre and shore. The highest LSI values are observed in summer, which is indicative of strong land-affected signal (especially adjacency effects). The lowest LSI values are detected in winter, which indicates that during winter the land-affected signal is weaker than other seasons. The seasonal variation pattern of LSI is highly consistent among the four studied lakes. The absolute LSI values at Lake Ringsjön are lower when compared to the other three lakes for both MERIS RR and OLCI images. LSI values from OLCI images are lower than those from MERIS RR images, which have a coarser spatial resolution and are more likely influenced by the land-affected signal than OLCI images. Fig. 16 shows an example of the average LSI in four seasons for Lake Rusken. It clearly demonstrates the spatial changes of the land-affected signal in different seasons. For example, the extent of high LSI values (yellow) increases from spring to summer (Fig. 16a to 16b), and then shrinks from autumn to winter (Fig. 16c to 16d).

4. Discussion

4.1. Applicability of the proposed flagging method

In this study, we discriminate the spectral influence of land on R_w

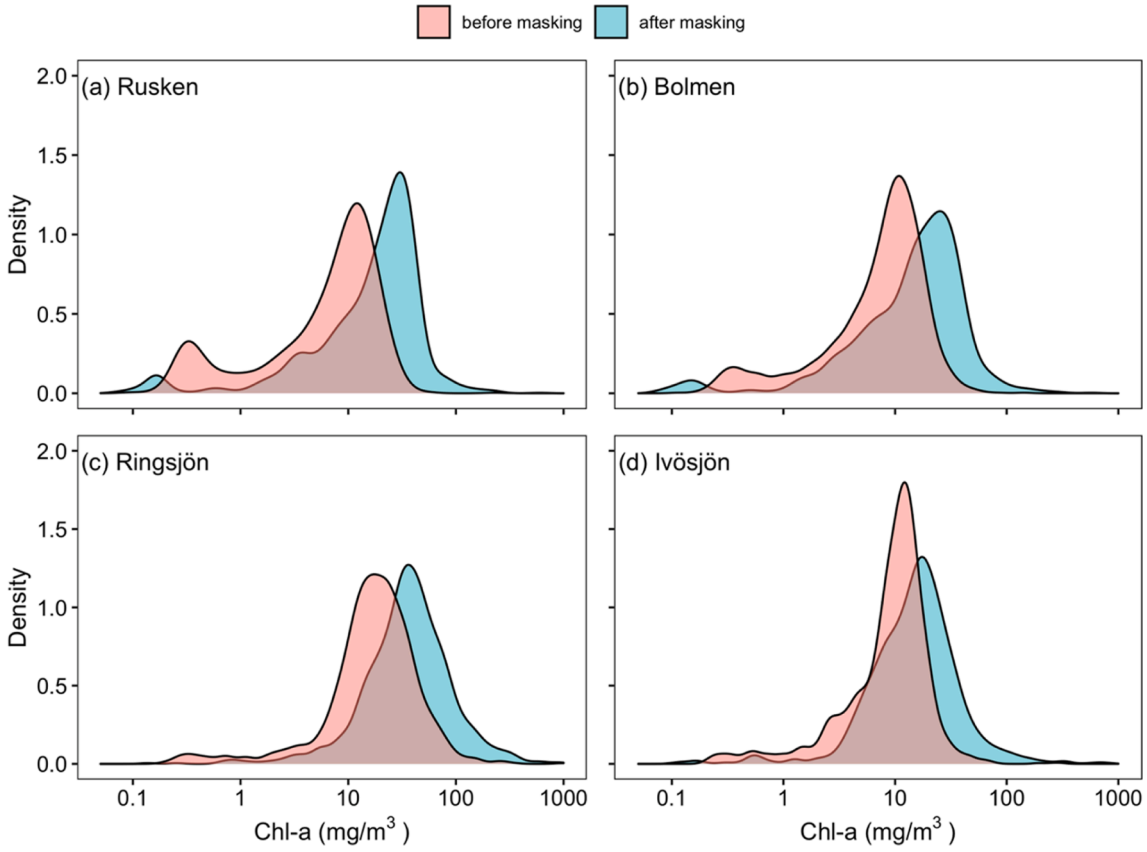

Fig. 12. Lake average Chl-a concentration before and after masking out land-affected pixels for (a) Lake Rusken, (b) Lake Bolmen, (c) Lake Ringsjön, and (d) Lake Ivösjön.

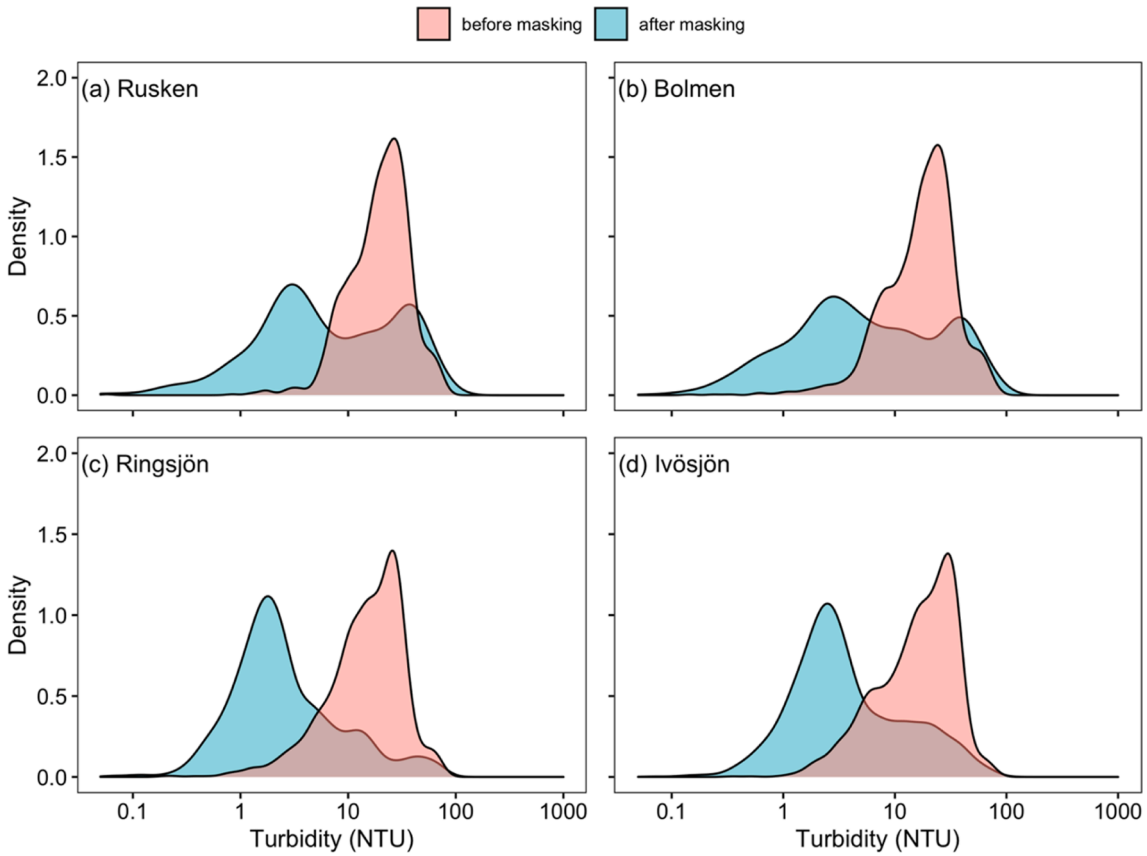

Fig. 13. Lake average turbidity before and after masking out land-affected pixels for (a) Lake Rusken, (b) Lake Bolmen, (c) Lake Ringsjön, and (d) Lake Ivösjön.

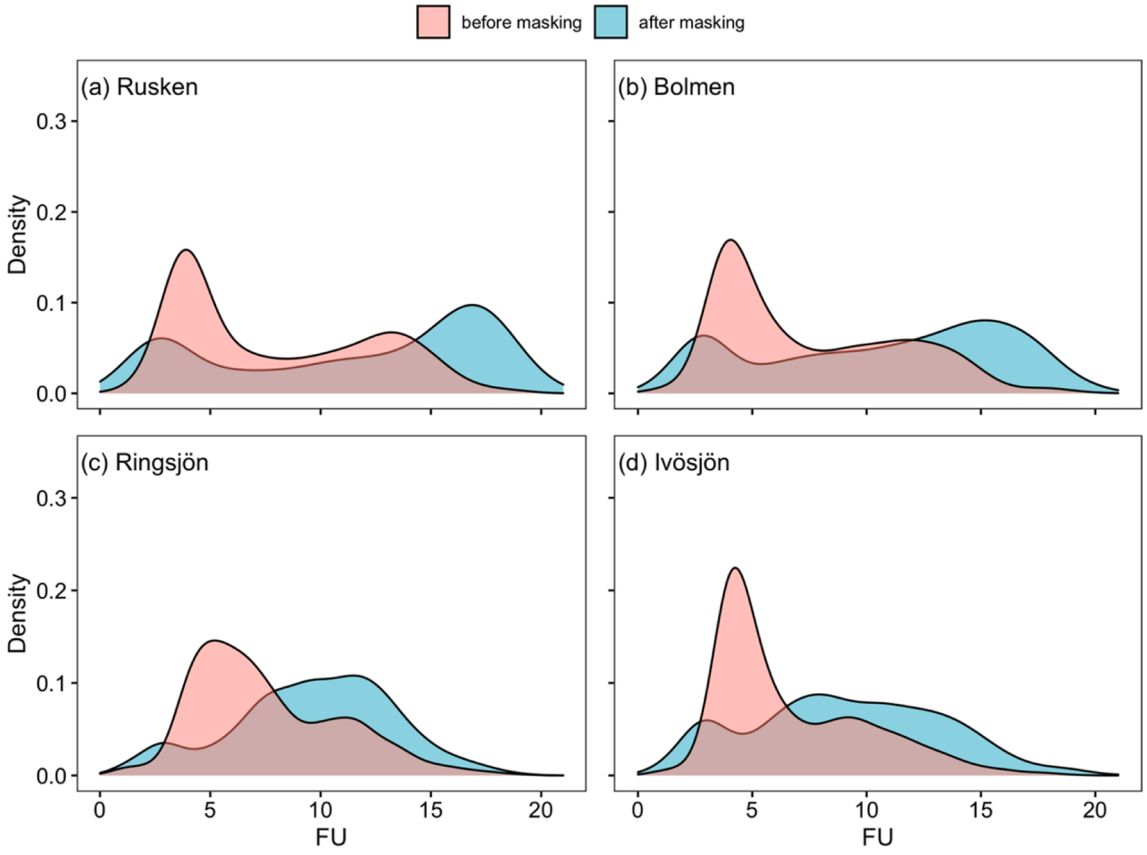

Fig. 14. Lake average FU before and after masking out land-affected pixels for (a) Lake Rusken, (b) Lake Bolmen, (c) Lake Ringsjön, and (d) Lake Ivösjön.

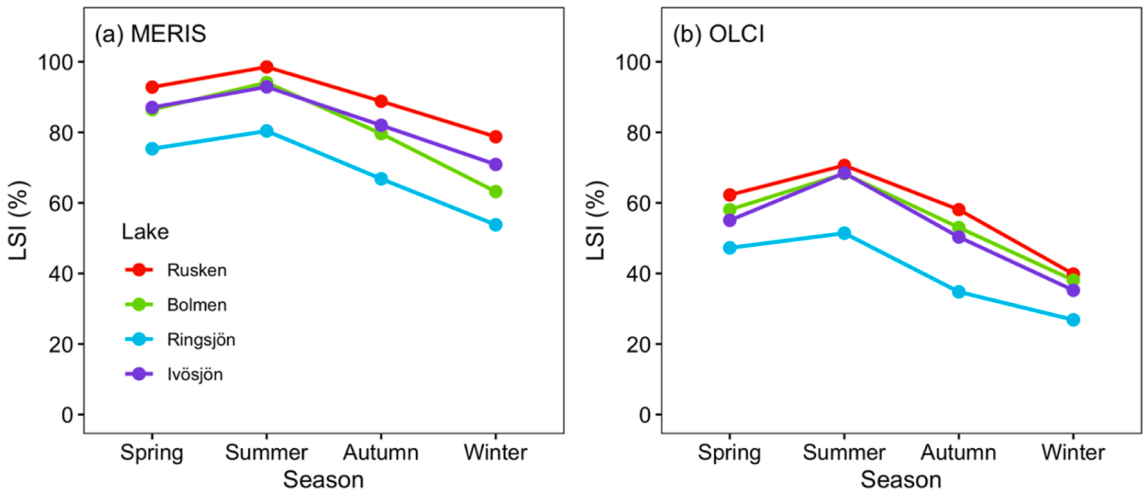

Fig. 15. Variation of mean LSI for the studied four lakes in different seasons. (a) Mean LSI from MERIS RR images. (b) Mean LSI from OLCI images.

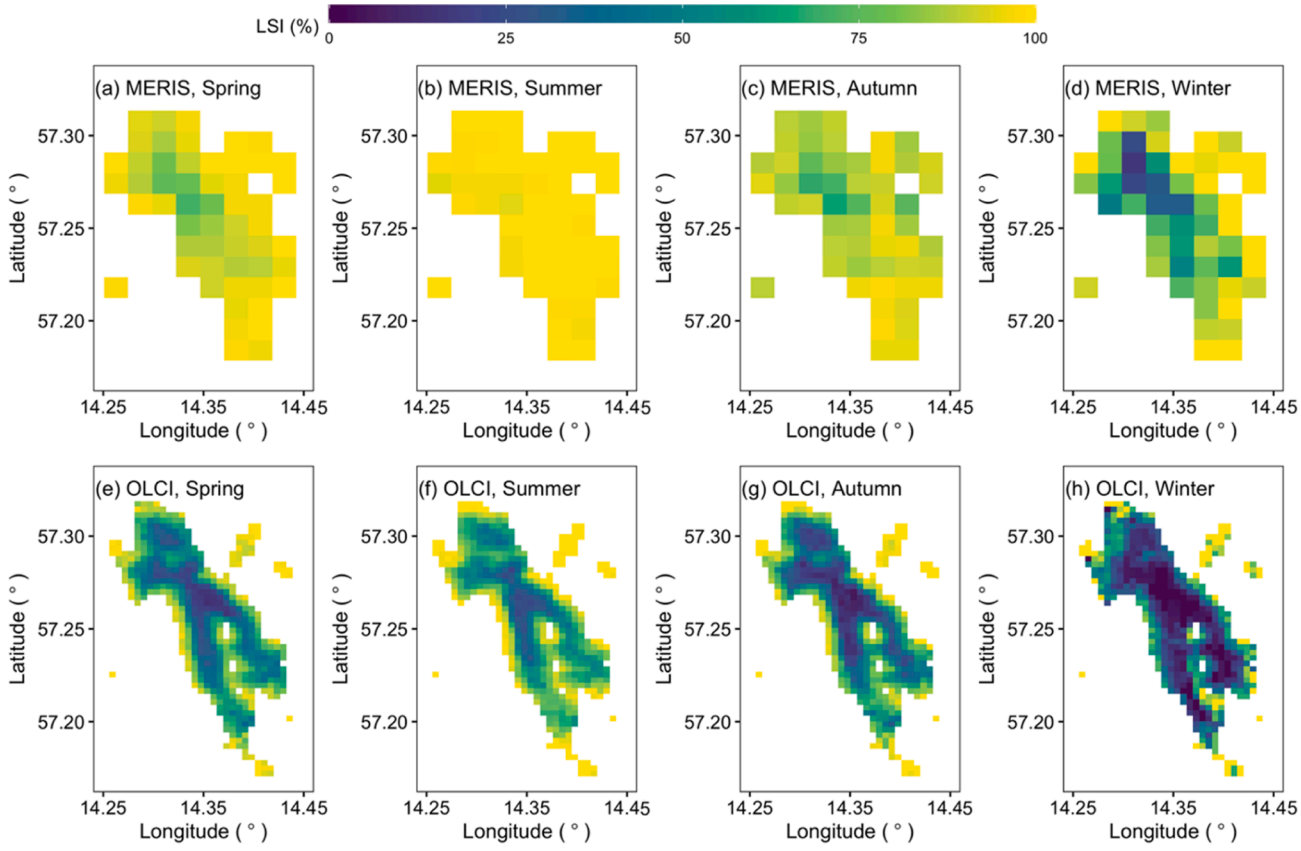

Fig. 16. Example of the seasonal variation of the frequency of observations with land-affected signals in Lake Rusken.

over a gradient from shoreline to lake centre. Using these spectral signatures in an OWT classification framework allows us to assess the severity of the influence by land-affected signals on the water observations. The usefulness of such a framework depends on its transferability to other water systems, whilst regional and temporal consistency is shown in this study. Specifically, the new OWTs developed based on observations from lakes Rusken and Bolmen in Sweden, are found to be applicable to datasets from lakes Ringsjön and Ivösjön. Our approach flags both pixels at the lake shore, where a mixing of land–water spectra is most likely, as well as a variable number of pixels between lake shore and lake centre because of adjacency effects (e.g., as shown in Fig. 2b and 7b). This, therefore, suggests a dynamic flagging of impacted observations is possible for each observed satellite scene, which can conserve a higher fraction of higher-quality observations than result from the application of static land masks (e.g., using LWF). The proposed approach has the additional benefit that it is adaptable to cope with a seasonally varying lake extent, which is not possible with a static land mask.

As expected, our results showed increasing LSI from lake centre to lake shore (Figs. 7–10) as has been shown in other studies in lakes as well (e.g., Kiselev et al., 2015). The dominant land cover surrounding the studied lakes is vegetation (Forest and arable land, O'Dwyer, 2019;

Klante et al., 2021), whilst snow cover may occur during December through April. Given that water efficiently absorbs light in the NIR, while vegetation has a high reflectance in the NIR, adjacency effects from surrounding vegetation or mixing of vegetation reflectance are likely to elevate the reflectance of water in the NIR wavelengths. The newly identified OWTs capture land-affected signal of which the main spectral feature is the high NIR reflectance (>700 nm), which agrees with previous research on adjacency effects by Tanré et al. (1987) in two lakes in North Carolina, and Kiselev et al. (2015) in Lake Constance.

The two new OWTs are added here to the existing set of 13 OWTs from Spyrakos et al. (2018), which are derived from in situ hyperspectral reflectance datasets. It has to be noted that the two new OWTs are for land-affected signal flagging purpose only, and they are not employed in water quality variable retrievals using blending algorithms. The new OWTs can equally be applied to other existing sets of OWTs too, and they may be used to isolate land-affected signals from satellite-derived OWT spectra which may already include effects of land, in order to better separate these effects. The approach suggested in this study can also be repeated with additional atmospheric correction models or sensors to identify sets of new OWTs that carry information of land-affected signals specific to those atmospheric correction models or observation conditions. As an example, we show that similar spatial patterns of LSI as in Fig. 7 for Lake Rusken are achieved using Rayleigh-corrected MERIS RR and OLCI images, by repeating the steps in Sections 2.4.2 and 2.4.3 (Fig. 17).

The proposed method in this study can also be used with additional conditions to deal with land-affected signal flagging in different lakes. For example, we found that some pixels in the centre of some large oligotrophic lakes are erroneously flagged as land-affected pixels (Müller et al., 2021). An additional test on the sum of membership scores of OWT-14 and OWT-15 (with pixels only flagged where this number exceeds 1.59) has been added to deal with this problem in the ESA Lake_cci v2.0 product (Carrea et al., 2022). However, this additional criterion provides less strict flagging in small northern lakes and limits the improvement of water colour and water quality products. It is therefore recommended to provide multiple options for application-dependent flagging, although a revision of the full set of OWTs as suggested above may provide a more consistent solution.

Comparison of the OWT-based flagging method with the method proposed by Matthews and Odermatt (2015) highlights some further improvements gained by the presently proposed method. Applying their method on MERIS RR and OLCI images in Lake Rusken, we have observed opposite spatial patterns (Fig. 18) compared to our results shown in Fig. 17. This is because the NDVI values of nearshore pixels are higher than the threshold of 0.2 for adjacency effects flagging in the previously published method, and those nearshore pixels are finally erroneously identified as floating materials (e.g., algal blooms, vegetation) other than adjacency effects.

4.2. Impacts on the retrieval of water quality variables

The land-affected signal can heavily influence the shape and magnitude of R_w spectra and thus introduce errors to the retrieval of water quality variables (Santer & Schmechtig, 2000; Giadino et al., 2007; Bulgarelli et al., 2018). Our results showed that land-affected signals can lead to biases in Chl-a and turbidity estimates (Figs. 11, 12 and 13). For example, nearshore pixels in Lake Bolmen have lower Chl-a and higher turbidity retrievals compared to pixels at lake centre (Fig. 19a, 19b). In this study, 52 % of the pixels of the four lakes are classified into OWT-3, OWT-9, OWT-10, or OWT-13, so the OC2 algorithm based on reflectance ratio between 490 and 560 nm has been used to derive the Chl-a concentration for those pixels (Liu et al., 2021). Land-affected signals lead to higher reflectance at 490 nm (Figs. 4 and 5), which increases the reflectance ratio between 490 and 560 nm (Fig. 19c), and finally leads to underestimation of Chl-a concentrations for land-affected pixels. There are 41 % of the pixels in this study classified into OWT-1, OWT-4, OWT-5 or OWT-6, where a NIR-Red algorithm based on Gons et al. (2005) has been used to estimate the Chl-a concentration. The land-affected signal elevates the NIR reflectance, which can lead to higher Chl-a estimations, but strong land-affected signals can also lead to negative Chl-a estimations because the R_w at 779 nm is too high (>0.137, Figs. 4 and 5). The single band centred around 709 or 754 nm are mainly used to derive turbidity in our studied lakes according to the OWT classification. The land-affected signal elevates the reflectance at these wavelengths, which in turn leads to higher turbidity retrievals (e.g., Lake Bolmen, Fig. 19b, 19d). In FU calculation, the increase of the reflectance ratio within the visible domain with higher values in the blue wavelengths (e.g., Fig. 19c) leads to higher hue

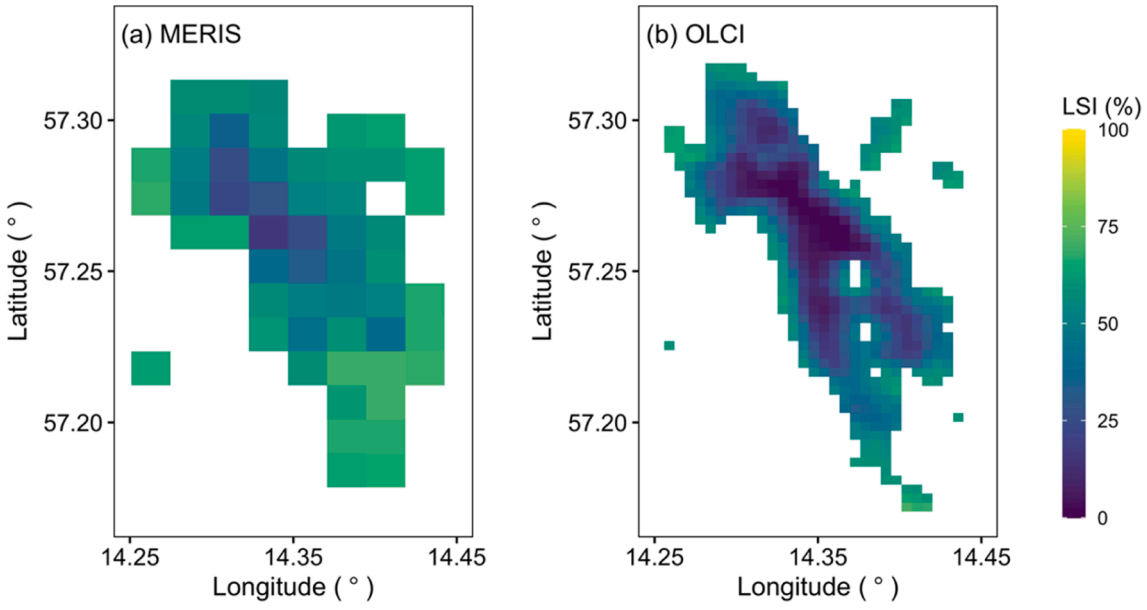

Fig. 17. Land-affected signal frequency maps detected in Lake Rusken using the framework proposed in this study, but the new OWTs (OWT-14, OWT-15) were determined from Rayleigh-corrected MERIS RR (2009–2011) and OLCI (2017–2019) images. The processing steps are otherwise the same as those described in sections 2.4.2–2.4.3.

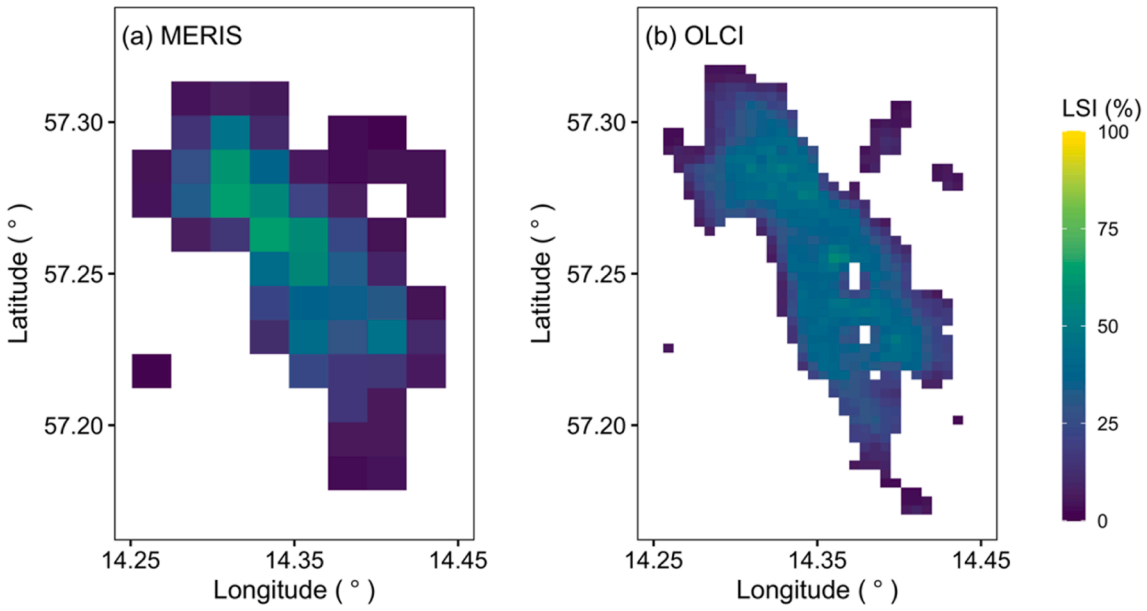

Fig. 18. Land-affected signal frequency maps in Lake Rusken detected from (a) MERIS RR (2009–2011) and (b) OLCI (2017–2019) images using the method proposed by Matthews and Odermatt (2015).

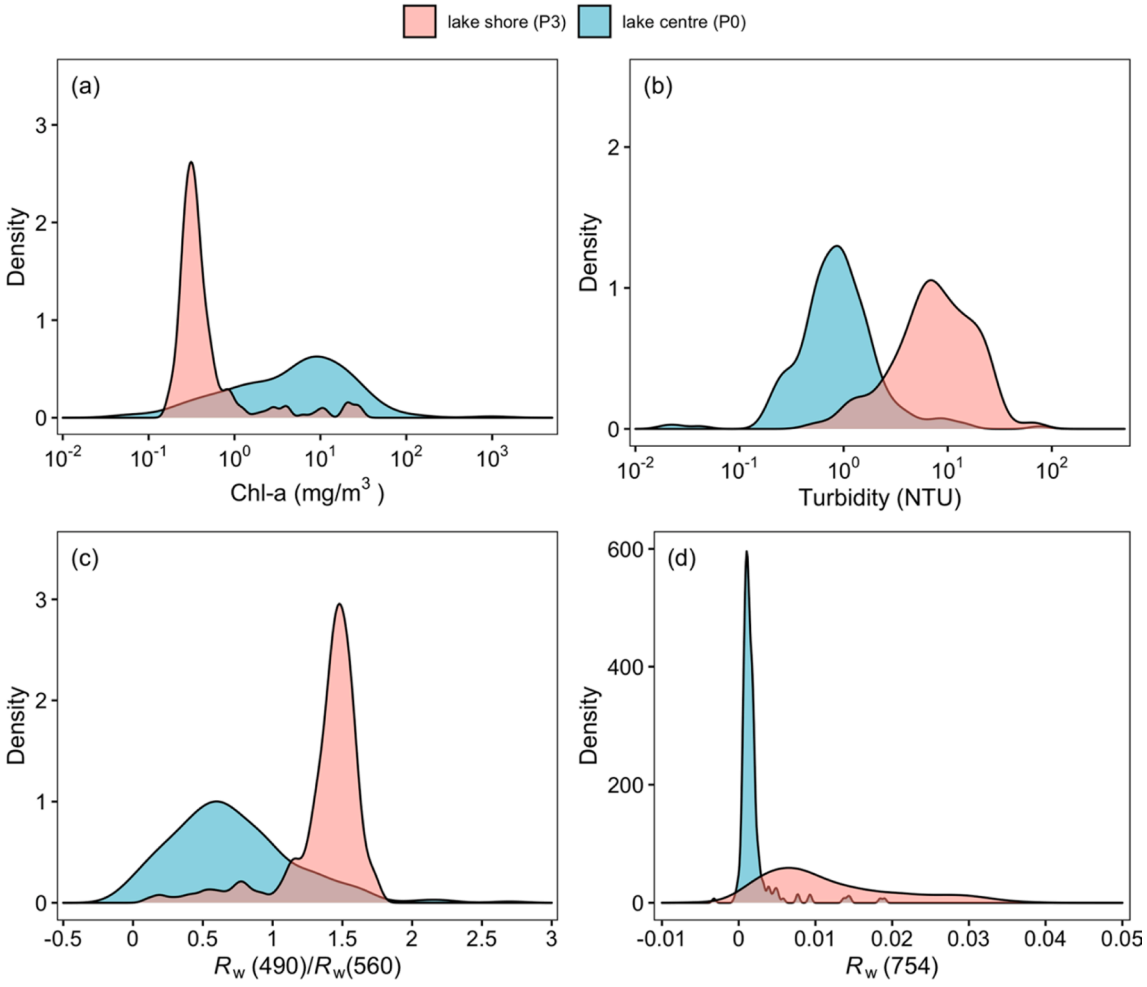

Fig. 19. Comparison of (a) Chl-a concentration, (b) turbidity, (c) $R_w(490)/R_w(560)$ ratio, (d) $R_w(754)$ between lake centre (P0) and lake shore (*P*3) of Bolmen, locations of P0 and *P*3 are same as those in Fig. 3.

angles, and therefore to lower FU. As it can be seen in Fig. 14, the calculated FU values increase after masking out land-affected pixels, i.e., water colour changes from indigo-blue to yellowish green or greenish brown. Because of known high coloured dissolved organic matters (CDOM) concentrations throughout the studied lakes, the FU values obtained after masking out land-affected pixels are considered more realistic.

4.3. Spatial and seasonal variability of the land-affected signal

The results in this study demonstrate the limitations of coarse sensors for monitoring small lakes, when the extent of the lake is covered by a small number of pixels. Even if those water bodies are observable by the sensor, their observations are more prone to suffer from land-affected signals. LSI for MERIS RR images (~1.2 km × 1.2 km spatial resolution, Fig. 7a, 8a, 9a, 10a) shows higher values than OLCI images (~300 m × 300 m spatial resolution, Fig. 7b, 8b, 9b, 10b). These sensors are otherwise optically similar, and the same waveband sets are used for the atmospheric correction. Only pixels at the very centre of the lakes show low LSI values in the MERIS RR images. In lower spatial resolution images, one pixel can cover a wider area, so the likelihood to contain signals from adjacent land are higher. Lower resolution images have typically higher signal to noise ratio (SNR), which is more likely to exceed the detection threshold of the land-affected signal, and thus they can be more sensitive to such as adjacency effects (Bulgarelli & Zibordi, 2018). Therefore, full resolution MERIS and OLCI images should be preferred for small inland waters. Unfortunately, MERIS FR archives do not have the same global coverage as MERIS RR (particularly during the first years of the operational phase), so that full climate data records have to combine both ideally.

Our results confirm links between lake shape (or coastline complexity) and frequency of the land-affected signal. LSI values at the centre of lake Ringsjön (Fig. 9) are clearly lower than the LSI values at the centre of the other three lakes (Figs. 7, 8, 10), which seems to be associated with differences in coastline complexity. Lakes Rusken (34 km^2) and Ringsjön (39 km^2) have similar surface area, whereas there are many scattered islands in Lake Rusken and only one small island in Lake Ringsjön. The shape of lake Ringsjön is rounder than lake Rusken, with maximum distances to land of 2.0 km and 1.4 km and perimeter/area (P/A) ratios of 1.79 and 2.95, respectively.

The land-affected signal shows a clear seasonal variability in all studied lakes, with the strongest effects in summer and the weakest effects in winter (Figs. 15 and 16). We found that this variability has a significant positive relationship with the surrounding NDVI ($R^2 = 0.44$ for MERIS, $R^2 = 0.74$ for OLCI, $P < 0.01$), and a negative relationship with sun zenith angle ($R^2 = 0.55$ for MERIS, $R^2 = 0.67$ for OLCI, $P < 0.01$) for the studied lakes. In summer, the sun zenith angle is lower (indicating higher light intensity and a shorter atmospheric path) and the surrounding vegetation is greener than in winter, thus there are more photons from nearby land pixels presenting more perturbation to the water pixels. However, because there are different number of available images in four seasons in the studied lakes (for MERIS: spring (N = 259), summer (N = 276), autumn (N = 210) and winter (N = 59); for OLCI: spring(N = 155), summer(N = 204), autumn (N = 126) and winter (N = 69)), snow or ice cover may also have potential impact on R_w. More specific studies on the seasonality of the land-affected signal and the factors influencing these seasonal variations are needed in the future.

4.4. Uncertainties from atmospheric correction

In this study, the spectral signatures for the land-affected signal are directly identified from atmospherically corrected satellite images. As shown in Fig. 6a, the POLYMER atmospheric correction produces some negatives values at 443 nm for OLCI, and between 650 and 700 nm for MERIS RR. Those negative values are possibly caused by adjacency effects (Sterckx et al., 2011; Sterckx et al., 2015) resulting in over-correction for atmospheric or glint components resolved in POLYMER. In addition, different spectral shape and magnitude are observed between MERIS RR and OLCI for the same lake (e.g., Fig. 4c and 4f). These differences may be caused by: (1) an inconsistency of the atmospheric correction accuracy between MERIS RR and OLCI because of the difference in band configuration; (2) the different levels of land-affected signals, i.e., MERIS RR with lower NIR reflectance might be less affected by land, and OLCI with higher NIR reflectance might be more affected by land. The above-mentioned reasons might finally lead to the two different OWTs in this study (OWT-14 and OWT-15). Our further tests have found that using both OWT-14 and OWT-15 for land-affected pixel flagging showed better results than only using one OWT, e.g., only OWT-14 for MERIS RR, or only OWT-15 for OLCI.

Atmospheric correction for inland waters remains a challenge (Palmer et al., 2015). Improvements of atmospheric correction methods are needed to address the consistency, stability and accuracy of long time series particularly at the global scale if regional adjustments to algorithms are not practicable. The definitions of OWTs and associated spectral signatures of land-affected signals allow for subtle adjustments to data flagging, masking and algorithm adjustments to be explored. We may consider to extend these definitions further with bottom reflectance effects, submerged and emergent vegetations or specific atmospheric disturbances (e.g., smoke, ash, pollen) in the future.

5. Conclusions

We have identified two new OWTs associated with land-affected signals from MERIS RR and OLCI images over Lake Rusken and Lake Bolmen in Sweden, which when added to a fuzzy OWT classification framework help to delineate the influence of nearby and sub-pixel land on water colour and water quality variable estimates. The identified new OWTs and proposed flagging method are transferable between four lakes in the same region in Sweden, ranging in shoreline complexity, density of islands and water colour. We conclude that (1) the OWT-based land-affected signal flagging method can provide reasonable flagging for remote sensing of inland waters; (2) the land-affected signal influences water colour and water quality variable estimates, which in this case leads to underestimation of Chl-a concentration and FU value, and overestimation of turbidity; (3) the land-affected signal shows clear seasonal variation, which is strongest in summer and weakest in winter, and associated with variations in land cover (NDVI) and illumination conditions (sun zenith angle); (4) coarser resolution satellite images are more likely to suffer from land-affected signal than finer resolution satellite images, particularly in small lakes.

CRediT authorship contribution statement

Dalin Jiang: Conceptualization, Data curation, Formal analysis, Methodology, Writing – original draft. **Jorrit Scholze:** Data curation, Formal analysis, Writing – review & editing. **Xiaohan Liu:** Data curation, Formal analysis, Writing – review & editing. **Stefan G.H. Simis:** Conceptualization, Writing – review & editing. **Kerstin Stelzer:** Funding acquisition, Writing – review & editing. **Dagmar Müller:** Writing – review & editing. **Peter Hunter:** Writing – review & editing. **Andrew Tyler:** Writing – review & editing. **Evangelos Spyrakos:** Conceptualization, Methodology, Writing – review & editing, Funding acquisition.

Declaration of Competing Interest

The authors declare that they have no known competing financial interests or personal relationships that could have appeared to influence the work reported in this paper.

Data availability

The authors do not have permission to share data.

Acknowledgements

This research was supported by European Space Agency (ESA) Climate Change Initiative Lakes_cci project. We thank ESA for providing satellite imagery, and the Miljödata MVM for providing in situ observation data from lakes Bolmen and Ringsjön. We also appreciate the editorial team and reviewers for their time and effort, valuable comments and suggestions.

References

Arzel, C., Nummi, P., Arvola, L., Pöysä, H., Davranche, A., Rask, M., Manninen-Johansen, S., 2020. Invertebrates are declining in boreal aquatic habitat: The effect of brownification? Sci. Total Environ. 724, 138199 https://doi.org/10.1016/j.scitotenv.2020.138199.

Balasubramanian, S.V., Pahlevan, N., Smith, B., Binding, C., Schalles, J., Loisel, H., Boss, E., 2020. Robust algorithm for estimating total suspended solids (TSS) in inland and nearshore coastal waters. Remote Sens. Environ. 246, 111768 https://doi.org/10.1016/j.rse.2020.111768.

Blaber, S.J., Cyrus, D.P., Albaret, J.J., Ching, C.V., Day, J.W., Elliott, M., Silvert, W., 2000. Effects of fishing on the structure and functioning of estuarine and nearshore ecosystems. ICES J. Mar. Sci. 57 (3), 590–602. https://doi.org/10.1006/jmsc.2000.0723.

Bulgarelli, B., Zibordi, G., 2018. Analysis of Adjacency Effects for Copernicus Ocean Colour Missions. *Publications Office of the European Union*, Luxemburg. https://doi.org/10.2760/178467.

Bulgarelli, B., Zibordi, G., Mélin, F., 2018. On the minimization of adjacency effects in SeaWiFS primary data products from coastal areas. Opt. Express 26 (18), A709–A728. https://doi.org/10.1364/OE.26.00A709.

Carrea, L.; Crétaux, J.-F.; Liu, X.; Wu, Y.; Bergé-Nguyen, M.; Calmettes, B.; Duguay, C.; Jiang, D.; Merchant, C.J.; Mueller, D.; Selmes, N.; Spyrakos, E.; Simis, S.; Stelzer, K.; Warren, M.; Yesou, H.; Zhang, D. (2022): ESA Lakes Climate Change Initiative (Lakes_cci): Lake products, Version 2.0. NERC EDS Centre for Environmental Data Analysis, 18 March 2022. 10.5285/ab8d21568c81491fbb9a300c36884af7.

Cui, T.W., Zhang, J., Wang, K., Wei, J.W., Mu, B., Ma, Y., Chen, X.Y., 2020. Remote sensing of chlorophyll a concentration in turbid coastal waters based on a global optical water classification system. ISPRS J. Photogramm. Remote Sens. 163, 187–201. https://doi.org/10.1016/j.isprsjprs.2020.02.017.

Edsall, T.A., Charlton, M.N., 1997. Nearshore waters of the Great Lakes. *Environment Canada and U.S. Environmental Protection Agency*. EPA, 905-R-97-015a.

Farr, T.G., Rosen, P.A., Caro, E., Crippen, R., Duren, R., Hensley, S., Alsdorf, D., 2007. The shuttle radar topography mission. Rev. Geophys. 45 (2) https://doi.org/10.1029/2005RG000183.

Giardino, C., Brando, V.E., Dekker, A.G., Strömbeck, N., Candiani, G., 2007. Assessment of water quality in Lake Garda (Italy) using Hyperion. Remote Sens. Environ. 109 (2), 183–195. https://doi.org/10.1016/j.rse.2006.12.017.

Gons, H.J., Rijkeboer, M., Ruddick, K.G., 2005. Effect of a waveband shift on chlorophyll retrieval from MERIS imagery of inland and coastal waters. (2005). J Plankton Res. 27 (1), 125–127. https://doi.org/10.1093/plankt/fbh151.

Jägerbrand, A.K., Brutemark, A., Sveden, J.B., Gren, M., 2019. A review on the environmental impacts of shipping on aquatic and nearshore ecosystems. Sci. Total Environ. 695, 133637 https://doi.org/10.1016/j.scitotenv.2019.133637.

Jerlov, N.G., 1977. Classification of sea water in terms of quanta irradiance. ICES J. Mar. Sci. 37 (3), 281–287. https://doi.org/10.1093/icesjms/37.3.281.

Jiang, D., Matsushita, B., Setiawan, F., Vundo, A., 2019. An improved algorithm for estimating the Secchi disk depth from remote sensing data based on the new underwater visibility theory. ISPRS J. Photogramm. Remote Sens. 152, 13–23. https://doi.org/10.1016/j.isprsjprs.2019.04.002.

Jiang, D., Matsushita, B., Pahlevan, N., Gurlin, D., Lehmann, M.K., Fichot, C.G., O'Donnell, D., 2021. Remotely estimating total suspended solids concentration in clear to extremely turbid waters using a novel semi-analytical method. Remote Sens. Environ. 258, 112386 https://doi.org/10.1016/j.rse.2021.112386.

Kirk, J.T.O., 1984. Dependence of relationship between inherent and apparent optical properties of water on solar altitude. Limnol. Oceanogr. 29 (2), 350–356. https://doi.org/10.4319/lo.1984.29.2.0350.

Kiselev, V., Bulgarelli, B., Heege, T., 2015. Sensor independent adjacency correction algorithm for coastal and inland water systems. Remote Sens. Environ. 157, 85–95. https://doi.org/10.1016/j.rse.2014.07.025.

Klante, C., Larson, M., Persson, K.M., 2021. Brownification in Lake Bolmen, Sweden, and its relationship to natural and human-induced changes. J. Hydrol.: Reg. Stud. 36, 100863 https://doi.org/10.1016/j.ejrh.2021.100863.

Klein, I., Gessner, U., Dietz, A.J., Kuenzer, C., 2017. Global WaterPack–A 250 m resolution dataset revealing the daily dynamics of global inland water bodies. Remote Sens. Environ. 198, 345–362. https://doi.org/10.1016/j.rse.2017.06.045.

Liu, X., Steele, C., Simis, S., Warren, M., Tyler, A., Spyrakos, E., Hunter, P., 2021. Retrieval of Chlorophyll-a concentration and associated product uncertainty in optically diverse lakes and reservoirs. Remote Sens. Environ. 267, 112710 https://doi.org/10.1016/j.rse.2021.112710.

Matsushita, B., Yang, W., Yu, G., Oyama, Y., Yoshimura, K., Fukushima, T., 2015. A hybrid algorithm for estimating the chlorophyll-a concentration across different trophic states in Asian inland waters. ISPRS J. Photogramm. Remote Sens. 102, 28–37. https://doi.org/10.1016/j.isprsjprs.2014.12.022.

Matthews, M.W., Odermatt, D., 2015. Improved algorithm for routine monitoring of cyanobacteria and eutrophication in inland and near-coastal waters. Remote Sens. Environ. 156, 374–382. https://doi.org/10.1016/j.rse.2014.10.010.

Moore, T.S., Dowell, M.D., Bradt, S., Verdu, A.R., 2014. An optical water type framework for selecting and blending retrievals from bio-optical algorithms in lakes and coastal waters. Remote Sens. Environ. 143, 97–111. https://doi.org/10.1016/j.rse.2013.11.021.

Morel, A., Prieur, L., 1977. Analysis of variations in ocean color 1. Limnol. Oceanogr. 22 (4), 709–722. https://doi.org/10.4319/lo.1977.22.4.0709.

Müller, D., Stelzer, K., Liu, X., Spyrakos, E., Jiang, D., 2021. CCN Consistency-Product Validation and Intercomparison Report for Consistency. ESA Lakes Climate Change Initiative. https://climate.esa.int/media/documents/CCI-LAKES-CCN-consistency_PVIR_1.2.pdf.

Neil, C., Spyrakos, E., Hunter, P.D., Tyler, A.N., 2019. A global approach for chlorophyll-a retrieval across optically complex inland waters based on optical water types. Remote Sens. Environ. 229, 159–178. https://doi.org/10.1016/j.rse.2019.04.027.

Odermatt, D., Danne, O., Philipson, P., Brockmann, C., 2018. Diversity II water quality parameters from ENVISAT (2002–2012): A new global information source for lakes. Earth Syst. Sci. Data 10 (3), 1527–1549. https://doi.org/10.5194/essd-10-1527-2018.

O'Dwyer, R., 2019. Land cover changes in Southern Sweden from the mid-Holocene to present day: insights for ecosystem service assessments. Geographical Information Science, Lund University. Master Thesis in.

Palmer, S., Kutser, T., Hunter, P.D., 2015. Remote sensing of inland waters: challenges, progress and future directions. Remote Sens. Environ. 157, 1–8. https://doi.org/10.1016/j.rse.2014.09.021.

Qing, S., Cui, T., Lai, Q., Bao, Y., Diao, R., Yue, Y., Hao, Y., 2021. Improving remote sensing retrieval of water clarity in complex coastal and inland waters with modified absorption estimation and optical water classification using Sentinel-2 MSI. Int. J. Appl. Earth Obs. Geoinf. 102, 102377 https://doi.org/10.1016/j.jag.2021.102377.

Santer, R., Schmechtig, C., 2000. Adjacency effects on water surfaces: primary scattering approximation and sensitivity study. Appl. Opt. 39 (3), 361–375. https://doi.org/10.1364/AO.39.000361.

Simis, S., N. Selmes, B. Calmettes, C. Duguay, C. J. Merchant, E. Malnes, H. Yésou, and P. Blanco. (2020). ESA Lakes Climate Change Initiative (Lakes_cci): Product User Guide.

Spyrakos, E., O'donnell, R., Hunter, P.D., Miller, C., Scott, M., Simis, S.G., Tyler, A.N., 2018. Optical types of inland and coastal waters. Limnol. Oceanogr. 63 (2), 846–870. https://doi.org/10.1002/lno.10674.

Steinmetz, F., Deschamps, P.Y., Ramon, D., 2011. Atmospheric correction in presence of sun glint: application to MERIS. Opt. Express 19 (10), 9783–9800. https://doi.org/10.1364/OE.19.009783.

Sterckx, S., Knaeps, S., Kratzer, S., Ruddick, K., 2015. SIMilarity Environment Correction (SIMEC) applied to MERIS data over inland and coastal waters. Remote Sens. Environ. 157, 96–110. https://doi.org/10.1016/j.rse.2014.06.017.

Sterckx, S., Knaeps, E., Ruddick, K., 2011. Detection and correction of adjacency effects in hyperspectral airborne data of coastal and inland waters: The use of the near infrared similarity spectrum. Int. J. Remote Sensing 32 (21), 6479–6505.

Taipale, S.J., Vuorio, K., Strandberg, U., Kahilainen, K.K., Järvinen, M., Hiltunen, M., Kankaala, P., 2016. Lake eutrophication and brownification downgrade availability and transfer of essential fatty acids for human consumption. Environ. Int. 96, 156–166. https://doi.org/10.1016/j.envint.2016.08.018.

Tanré, D., Deschamps, P.Y., Duhaut, P., Herman, M., 1987. Adjacency effect produced by the atmospheric scattering in thematic mapper data. J. Geophys. Res. Atmos. 92 (D10), 12000–12006. https://doi.org/10.1029/JD092iD10p12000.

Vadeboncoeur, Y., McIntyre, P.B., Vander Zanden, M.J., 2011. Borders of biodiversity: life at the edge of the world's large lakes. Bioscience 61 (7), 526–537. https://doi.org/10.1525/bio.2011.61.7.7.

Wang, S., Li, J., Zhang, B., Spyrakos, E., Tyler, A.N., Shen, Q., Peng, D., 2018. Trophic state assessment of global inland waters using a MODIS-derived Forel-Ule index. Remote Sens. Environ. 217, 444–460. https://doi.org/10.1016/j.rse.2018.08.026.

Wei, J., Lee, Z., Shang, S., 2016. A system to measure the data quality of spectral remote-sensing reflectance of aquatic environments. J. Geophys. Res. Oceans 121 (11), 8189–8207. https://doi.org/10.1002/2016JC012126.

Woerd, H.J., Wernand, M.R., 2015. True colour classification of natural waters with medium-spectral resolution satellites: SeaWiFS, MODIS. MERIS and OLCI. *Sensors* 15 (10), 25663–25680. https://doi.org/10.3390/s151025663.

Yamazaki, D., Trigg, M.A., Ikeshima, D., 2015. Development of a global~ 90 m water body map using multi-temporal Landsat images. Remote Sens. Environ. 171, 337–351. https://doi.org/10.1016/j.rse.2015.10.014.